

Lumbar Bone Mineral Density Estimation from Chest X-ray Images: Anatomy-aware Attentive Multi-ROI Modeling

Fakai Wang*, Kang Zheng, Le Lu, *Fellow, IEEE*, Jing Xiao, Min Wu, *Fellow, IEEE*, Chang-Fu Kuo* and Shun Miao

Abstract—Osteoporosis is a common chronic metabolic bone disease that is often under-diagnosed and under-treated due to the limited access to bone mineral density (BMD) examinations, e.g., via Dual-energy X-ray Absorptiometry (DXA). In this paper, we propose a method to predict BMD from Chest X-ray (CXR), one of the most commonly accessible and low-cost medical imaging examinations. Our method first automatically detects Regions of Interest (ROIs) of local and global bone structures from the CXR. Then a multi-ROI deep model with transformer encoder is developed to exploit both local and global information in the chest X-ray image for accurate BMD estimation. Our method is evaluated on 13719 CXR patient cases with their ground truth BMD scores measured by gold standard DXA. The model predicted BMD has a strong correlation with the ground truth (Pearson correlation coefficient 0.889 on lumbar 1). When applied for osteoporosis screening, it achieves a high classification performance (AUC 0.963 on lumbar 1). As the first effort in the field using CXR scans to predict the BMD, the proposed algorithm holds a strong potential in early osteoporosis screening and public health promotion.

Index Terms—Bone Mineral Density Estimation, Chest X-ray Imaging, Deep Self-Attention, Multi-ROI Modeling.

I. INTRODUCTION

OSTEOPOROSIS is the most common chronic metabolic bone disease, characterized by low bone mineral density (BMD) and decreased bone strength to resist pressure or squeezing force. With an aging population and longer life span, osteoporosis is becoming a global epidemic, affecting more than 200 million people worldwide [1]. Osteoporosis increases the risk of fragility fractures, which is associated with disability, fatality, reduced life quality, and financial burden to the family and the society. While with an early diagnosis and treatment, osteoporosis can be prevented or managed, osteoporosis is often under-diagnosed and under-treated among the population at risk [2]. More than half of insufficiency fractures occur in individuals who have never been screened for osteoporosis [3]. The under-diagnosis and under-treatment of osteoporosis are mainly due to 1) low

osteoporosis awareness and 2) limited accessibility of Dual-energy X-ray Absorptiometry (DXA) examination, which is currently the recommended modality to measure BMD.

Opportunistic screening of osteoporosis is an emerging research field in recent years [4]–[7]. It aims at reusing medical images originally used for other indications to screen for osteoporosis, which offers an opportunity to increase the screening rate at no additional cost and time. Previous attempts mainly focused on using the CT attenuation (i.e., Housefield Unit) of the vertebrae to correlate with BMD and/or fracture risk. As the most common prescribed medical image scanning, plain films have much greater accessibility than CT scans. Its excellent spatial resolution permits the delineation of fine bony micro-structure that may contain information that correlates well with the BMD. We hypothesize that specific regions of interest (ROI) in the standard chest X-rays (CXR) may help the opportunistic screening for osteoporosis.

In this work, we introduce a method to estimate the BMD from CXR to screen osteoporosis. Our method first locates anatomical landmarks of the patient’s bone structures and extracts multiple ROIs that may provide imaging biomarkers for osteoporosis. We propose a novel network architecture that jointly processes the ROIs with automatic feature weight adjustment to accurately estimate the BMDs. We experiment on 13719 CXRs with paired DXA BMDs (ground truth). Our best model achieves a high correlation with the DXA BMD (i.e., r-value 0.889 on lumbar 1), and an high AUC score for osteoporosis diagnosis (0.963 on lumbar 1, using T-score of -2.5 as threshold). This paper is extended from a preliminary work [8].

In summary, our contributions are three-fold: 1) to our best knowledge, we are the first to develop models using CXR to estimate BMD, which could serve as a practical solution for opportunistic screening of osteoporosis; 2) we propose the anatomy-aware Attentive Multi-ROI model to combine global and local information in CXR for accurate BMD estimation. 3) we demonstrate that our method achieves clinically useful osteoporosis screening performance.

II. RELATED WORK

A. Bone Mineral Density estimation and early screening

Currently bone mineral density examination via DXA machines is essential for osteoporosis determination and fracture risk assessment. In practice, bone densities of young adult are

Fakai Wang and Min Wu are with ECE Department, University of Maryland, College Park, MD 20742, USA. (email:jackwangumd@gmail.com). Kang Zheng is with PAII Inc., Bethesda, MD 20817, USA. Le Lu is with Alibaba Group DAMO Academy, New York, NY 10014, USA. Shun Miao is with Xpeng Motors, San Diego, CA, USA.

Jing Xiao is with Ping An Technology, Shenzhen, 510852, China.

Chang-Fu Kuo is with Chang Gung Memorial Hospital, Linkou, Taiwan, ROC. (email:zandis@gmail.com)

This work was partially done when Fakai Wang was an intern at PAII Inc. Chang-Fu Kuo and Fakai Wang are the corresponding authors.

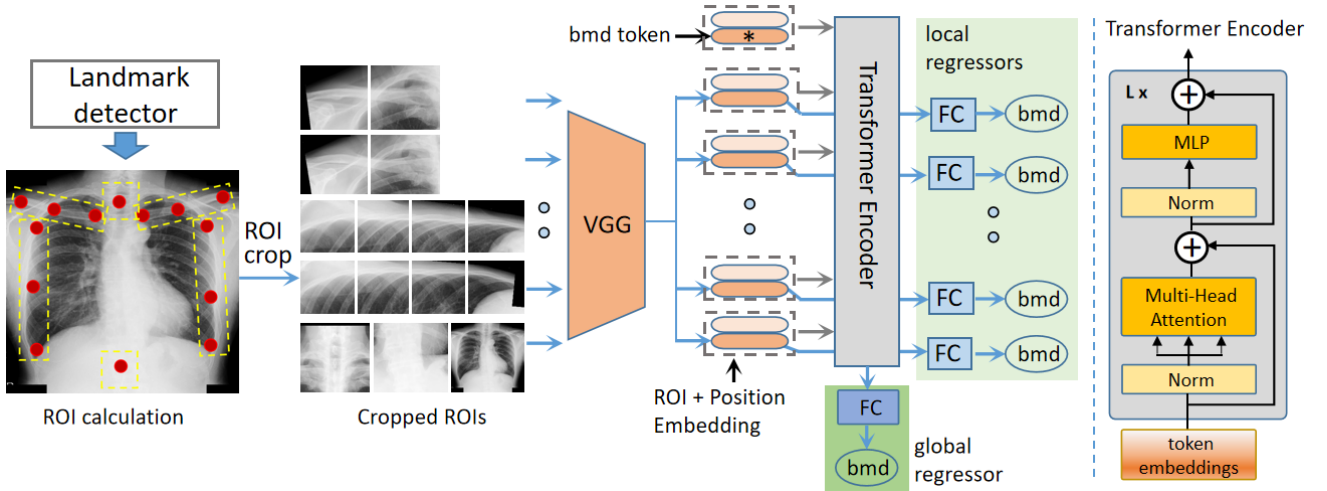


Fig. 1. The working pipeline of the proposed model. The landmark detector locates key bone points (red dots) on CXR images, then we crop and normalize 14 ROIs. These modalities go through a shared feature extractor (VGG16). The global regressor (dark green) works on global feature generated by the Transformer Encoder (grey). During training, results of both the local regressors (light green) and global regressor are used for loss calculation and back propagation.

used as reference and their bone density standard deviations (SD) are used as measuring unit (T-score) [9]. 1 unit of the T-score represent 1 unit of SD of the density, and 0 T-score represents the mean density of all the references. T-score at the spine, hip or mid-radius lower than -2.5 is considered osteoporosis. T-score between -2.5 and -1 is considered osteopenia, and T-score above -1 is considered normal. The current guideline advises people having symptoms or at risk to take the DXA BMD examination, which has many short-comings. First and foremost, DXA services are not widely available and could not be used as a general opportunistic screening technique. Second, the DXA score based diagnosis could not ensure accurate bone quality evaluation, since more fractures occur without reaching the severity of the osteoporosis [10] [3], due to the complex causes and symptoms of fracture. While the bone mineral density scores could not evaluate the bone structural hardness, the trabecular bone score (TBS) could provide bone microarchitecture and skeletal information [11] [12] [13]. However the TBS also requires the lumbar DXA scanning.

To promote fracture prevention without relying heavily on DXA services, opportunistic osteoporosis screening from common examinations other than DXA has been introduced. Firstly, the Quantitative Computed Tomography (QCT), as a common scanning in abdomen or chest for various diseases, can be re-used to determine osteoporosis without additional radiation exposure or cost [14] [15] [16] [17] [18]. The *Hounsfield Units* of the QCT scans have been shown to correlate well with DXA BMD scores for low BMD diagnosis [15] [19]. Elena Alacreu *et al* [19] reuse abdominal computed tomography scans performed in oncologic patients for the early detection of osteoporosis. QCT has the advantage of the three-dimensional assessment of the structural and geometric properties of the examined bone [20].

Secondly, the Quantitative Ultra Sound (QUS) based techniques for osteoporosis screening have drawn attention be-

cause of its safety, low cost, operating flexibility [20] [21] [22]. X-ray based examinations (DXA, QCT) have ionizing radiation which may not be suitable on sensitive population such as young children or the pregnant. DXA or CT machines occupy extensive space and require specially trained operators, limiting their availability and applicability for general screening. Quantitative Ultra Sound avoid these shortcomings, but QUS methods do not have standards on skeletal measuring site, performance criteria, or normative reference data in the clinical setting [21].

Lastly, the plain film or X-ray, as the most common radiography examination, can also be utilized for osteoporosis screening. The existing techniques (DXA, QCT, QUS) all work on specific bone regions and concern on the score from areal or volumetric mass. The X-ray images however contain not only the bone textures but also the contexts in larger spatial ranges. Since osteoporosis is metabolic bone disease which have complex manifestation on bone texture, involving a larger context enables the density relation capture which benefits bone density estimation. BMD analysis from the hip X-ray [23] have been verified to be helpful in opportunistic osteoporosis screening. In this paper, we focus on utilizing chest X-ray for opportunistic osteoporosis diagnosis and alarming. We investigate the input modality, model architectures, and prediction applicability.

B. Convolutional neural network and self-attention mechanism

Convolutional Neural Networks (CNN) have succeeded in natural vision tasks [24] [25] [26] [27] as well as in medical image analysis [28] [29] [30] [31]. Carefully curated stacks of CNN layers enable desired feature representation with good generalization, partly because the hierarchical characteristics of general visual patterns echo the inductive biases learnt by CNN layers. However, the inductive biases including translation equivalence and locality are less important for BMD

pattern learning. The texture contrast among neighboring pixels and regions have more BMD cues. But the CNN backbones such as Resnet, VGG fail to compare regional contextual information. They only operates on a local neighbourhood, ignoring global information during the layer operations [32] [33] [34].

Some papers exploit textual relationship by enhancing the quality of spatial CNN encodings in the feature hierarchy [32] or through dynamic channel-wise feature recalibration [35]. CCNet [36] propose the criss-cross attention module operating on each pixel to harvest the contextual information on the criss-cross path. LR-Net [37] presents the local relation layer (Local Relation Network) that adaptively determines aggregation weights based on the compositional relationship of local pixel pairs, enabling higher-level visual entity inference efficiently. GCNet [38] unifies the simplified non-local network [32] and SENet [35] into a general framework for global context modeling. The *object relation module* [39] models the object candidate relations through simultaneous interaction between appearance feature and geometry, enabling end-to-end object detection.

Inspired by the *Transformer* success in language tasks [40] [41] [42] [43], emerging works employ the *Transformer* modules to replace or facilitate the convolutional layers for visual tasks [34] [39] [44] [45]. The *Transformer Encoder* learns the global relationship through repetitive layers of *Multi-Head Self-attention* and *Multi-Layer Perception* operations. Attention Augmentation [33] augments convolutional operators with self-attention mechanism by concatenating convolutional feature maps with a set of self-attention feature maps. The iGPT [46] train the transformer model [42] on pixel sequences to generate coherent image completions in unsupervised settings where learnt feature representations are on par with CNN models. Given large amount of unlabeled training data, the ViT [34] apply a pure transformer architecture on image patches to surpass CNN backbones on image classification benchmarks.

A mindfully tailored combination of the CNN and Transformer could harness their strengths for our task. Convolutional layers can capture inductive biases such as translation equivariance and locality, while transformer encoder enables global feature interaction. The CXR BMD task requires the model to capture both local textures and regional relations automatically. Therefore, we employ both the convolutional feature extractor and self-attention fusion module in our proposed *Attentive Multi-ROI* model. Operating on the chest X-ray scanning, our method produces promising results for early osteoporosis diagnosis and warning.

III. METHODOLOGY

A. Problem Overview

In our opportunistic screening setting, the model input is a chest X-Ray image. Our goal is to predict the BMD of lumbar vertebrae (L1, L2, L3, L4), alarming the patient of possible low BMD or osteoporosis conditions. Our hypothesis is that the BMD information lies in the patterns in the chest X-ray, both in individual bone textures (local information)

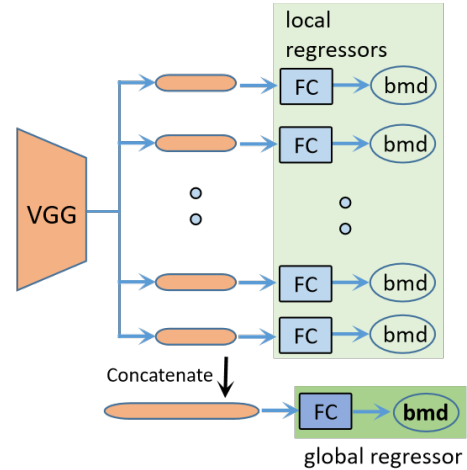


Fig. 2. The plain fusion process in the Multi-ROI model without global attention. Individual feature vectors are concatenated as the global representation, which goes through the global regressor (dark green).

and in the overall combination of chest bone contexts (global information). Directly feeding the whole chest image into a CNN model for BMD prediction (**Baseline**) is intuitive and viable, but it lacks localized and contrastive bone information among the chest regions. The proposed pipeline in Figure 1 consists of chest landmark detection, bone region of interest cropping, local texture extraction, global feature fusion, bone mineral density regression. We get the key landmarks for the chest from a Graph Convolution Network (GCN) model [47]. Then bone regions are cropped accordingly and fed into the proposed Attentive Multi-ROI model. The CNN layers learn local textures and patterns, extracting the individual features. Working on local feature embeddings, the Transformer Encoder refines individual representations to enable inter-regional feature interaction. At the end of the pipeline, local regressors and global regressor make BMD predictions on different levels of features respectively.

B. Automatic ROI Extraction

As the first step for our proposed pipeline, bone selection and region cropping prepare the model inputs. Although all bones could provide the density information due to the metabolic characteristics, the model should focus on the most effective and efficient regions. There are multiple bones in the chest area, bearing varied importance for BMD prediction. It is also unclear if the combination of distinct bone patterns are more effective. To enable representation learning of the local bone textures and to enable correlation exploration among different regions, landmarks of key bones are needed for the corresponding ROI extraction. Medical experts advise us to focus on clavicle bone, cervical vertebra, lumbar vertebra, ribcage edges. We avoid the central part of the chest X-ray where cardiac or pulmonary diseases may significantly influence the appearance. In the end, our model works on the ROI croppings of left/right clavicle bones, cervical spine, left/right rib-cage area, T12 vertebra.

We employ the graph-based landmark detector, Deep Adaptive Graph (DAG) [47] to automatically detect key landmarks

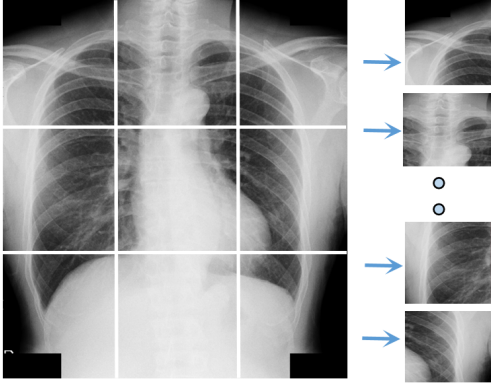


Fig. 3. Patch generation for input preparation of Attentive Multi-Patch model. The CXR image is separated into 3×3 non-overlapping regions.

in the chest. We identify 16 landmarks in Figure 1, which include 1) 3 points on the left/right clavicles, 2) 4 points along the left/right rib cages, 3) 1 point on the C7 vertebrae in cervical spine, 4) 1 point on the T12 vertebra. We manually labeled 1000 cases (16 landmarks on each CXR scan) as the training samples for the DAG model. The resulting landmark detector can reliably extract all the keypoints. Given the keypoints for each bone, we crop the corresponding bone regions. However, different bones have distinct shape and size, so we further sub-split the wider and higher regions. As seen in the resulting cropped ROIs 1, there are 2, 2, 4, 4, 1, 1 croppings for left clavicle, right clavicle, left ribcage, right ribcage, cervical, lumbar respectively. The cropping arrangements are based on the bone size and width/height ratio. Besides these 14 local ROIs, we also include the whole CXR image in the input. These 15 ROIs are resized and normalized before going through CNN layers.

C. Hybrid architecture of convolution and self-attention operations

VGG16 is used as the feature extractor in the proposed model. To utilize all the relevant information in the cropped ROIs, we need to effectively extract local patterns separately for each bone regions, which preserves the osteoporosis characteristics. Since there is little variation in the bone outlines for different people, the shape appearances do not tell much about BMD. Instead, finer level texture and pixel density around the bones keep the distinctions between the normal and the osteoporosis. So we extract the feature independently for each cropped ROI by applying convolutional backbone. VGG16 is better than more complex backbones because of its relative shallow layer depth which fits the simplicity of bone texture characteristics. We use *average_pool* to reduce the spatial dimensions on the VGG16 feature outputs, generating local representations \mathbf{f}_i , $i \in (1, \dots, N)$, $N=15$. However, the local textures and pattern combinations could have distinct manifestation in different people for the same BMD value [10] [9]. To make reliable density prediction, it should be addressed from the global level to account for the manually intractable variations resulting from disease causes, symptoms, complications, noises.

We employ the *Transformer Encoder* (grey box in Figure 1) for the global feature integration. The feature fusion process adjusts the individual features through layers of Multi-head Self-Attention (MSA) and Multiple Linear Perception (MLP) units, where the weighted relations are learnt automatically. In Equation 1, \mathbf{f}_i is the feature representation for the i th ROI, \mathbf{E}_{bmd} is the learnable *bmd token* (orange box with * inside in Figure 1), \mathbf{E}_{pos} represent $N=16$ learnable positional embeddings, \mathbf{z}_0 is the initial embeddings fed into the transformer encoder. Similar to *BERT*'s [*class token*], we prepend a learnable *bmd token* embedding \mathbf{E}_{bmd} as the target holder. The learnable position embeddings \mathbf{E}_{pos} are essential to keep spatial identity during the self-attention computation since there is no explicit sequential or grammatical order in the visual patches. In Equation 2 and 3, the alternating operations of MSA and MLP refine the feature representations. In our proposed model the encoder consists of $L=6$ layers similar to [34]. And each layer consists of *Layer Norm*, *MSA*, *Layer Norm*, *MLP*. In Equation 4, the *mean* of the adjusted feature embeddings are used as the global feature representation.

$$\mathbf{z}_0 = [\mathbf{E}_{bmd}; \mathbf{f}_1; \mathbf{f}_2; \dots; \mathbf{f}_N] + \mathbf{E}_{pos} \quad (1)$$

$$\mathbf{z}'_l = MSA(LN(\mathbf{z}_{l-1})) + \mathbf{z}_{l-1}, \quad l = 1 \dots L \quad (2)$$

$$\mathbf{z}_l = MLP(LN(\mathbf{z}'_l)) + \mathbf{z}'_l, \quad l = 1 \dots L \quad (3)$$

$$\mathbf{f}_{global} = \frac{1}{N} \sum_{i \in 1, \dots, N} \mathbf{z}_L^i \quad (4)$$

The core module of the transformer encoder is the *Multi-head Self-Attention*, illustrated in the *QKV* form in Equation 5-8. In Equation 5, $\mathbf{z} \in \mathbb{R}^{N \times D}$ is the feature embedding, the *query* (\mathbf{q}), *key* (\mathbf{k}), *value* (\mathbf{v}) are the projection of embedding \mathbf{z} on matrix mapping \mathbf{U}_{qkv} . $k = 6$ is the *head* number, $D_h = D/k$ is the feature size in each head. In Equation 6, A is the weight matrix and A_{ij} represents the pairwise similarity between the i th and the j th features. In Equation 6 and 7, the Self-Attention (SA) module adjust feature embedding according to weighted affinity. Regions of higher correlation contribute more, and others share less feature exchange. In this way, the individual feature becomes more robust to disease variation or noises. In the transformer encoder layer, the MLP consists of two linear layers with one non-linear *GELU* layer. The Transformer Encoder modules uses constant latent vector size $D=512$ through all of its layers, which is of the same size as VGG16 feature. The Layer Norm (LN) and residual connections are applied before and after every block respectively, which keep the training stable.

$$[\mathbf{q}, \mathbf{k}, \mathbf{v}] = \mathbf{z} \mathbf{U}_{qkv} \quad \mathbf{U}_{qkv} \in \mathbb{R}^{D \times 3D_h} \quad (5)$$

$$A = softmax(\mathbf{q} \mathbf{k}^T / \sqrt{D_h}) \quad A \in \mathbb{R}^{N \times N} \quad (6)$$

$$SA(\mathbf{z}) = A \mathbf{v} \quad (7)$$

$$MSA(\mathbf{z}) = [SA_1(\mathbf{z}); SA_2(\mathbf{z}); \dots; SA_k(\mathbf{z})]\mathbf{U}_{msa} \quad (8)$$

$$\mathbf{U}_{msa} \in \mathbb{R}^{k \cdot D_h \times D}$$

D. BMD Estimation via Joint Analysis of the ROIs

We apply local regressors and global regressor on the extracted local features $\mathbf{f}_i, i \in 1, \dots, N$ and aggregated global feature \mathbf{f}_{global} respectively for BMD prediction. In Figure 1, we employ separate *FC* regressors for different local ROIs. All the regressors consist of two linear layers and one *ReLU* non-linear layer. We employ L2 loss on the predictions. The local regressions are active during training iterations to regularize feature representations but ignored during evaluation, while the global regression is used all the time. During validation or inference, only the global BMD output is used. By jointly utilizing the global and local ROIs in the chest and jointly promoting feature exchange through the transformer encoder, the network is capable of extracting BMD patterns on different scales for robust regression.

E. Implementation Details

We trained our model on a workstation with Intel Xeon W-2295 CPU @ 3.00GHz, 132 GB RAM, and 4 NVIDIA Quadro RTX 8000 GPUs. Our models are implemented with PyTorch. The input images/ROIs sizes are set as (256, 256) by default which has the best results. The training augmentations include scaling, rotation, translation, random flip. The SGD optimizer has a learning rate of 0.0001, a weight decay of 4e-4. All models are trained for 100 epochs. The four components in our model, VGG16 feature extractor, transformer encoder, local regressors, global regressors, occupy 14.8M, 7.9M, 2.1M, 0.13M parameters respectively, which sum to 25M parameters in total.

IV. EXPERIMENTS

A. Experiment Setup

Dataset. We collected 13719 frontal view CXR scans, with paired DXA BMD scores (on four lumbar vertebrae L1 - L4) as ground truth. The data come from *anonymous hospital* after de-identification of the patient privacy. All experiments use the same data split, with 8265, 2759 and 2695 patient cases for training, validation and testing, respectively. There is no patient overlapping between data splits.

Metrics. We evaluate our models on quantitative metrics essential to clinical verification and practical deployment. Our metrics include the *Root-Mean-Square Error* (RMSE), the *Pearson Correlation Coefficient* (R-value), *Area Under Curve* (AUC), sensitivity, specificity, coefficient of determination (R squared or R^2) of the linear fitting curve, standard deviation of the prediction errors. RMSE measures the root of averaged square differences between predicted value and ground truth. The R-value measures the linear correlation between the predicted and the ground truth, only considering the sequential correlation regardless the absolute values. For osteoporosis classification, BMD values are transformed into T-score values

by checking the transforming table in the DXA machine [9] [10]. In the T-score range, the AUC measures accumulated true positive (osteoporosis) rate under different judging thresholds for binary classification. The sensitivity, specificity are also for osteoporosis classification purpose. The linear fitting curve illustrates the overall correspondence direction and modeling quality. The coefficient of determinant quantifies the fitting goodness. We also draw the Bland-Altman plot and show the standard deviation.

B. Attentive Multi-ROI model performance

We train and test our proposed Attentive Multi-ROI (*AttMul-Roi*) model on four lumbar BMD tasks separately. The performance results are listed (as **Ours**) in Table I. On L1 and L2 tasks, the proposed model achieve high R-value (0.889, 0.889) and low RMSE (0.067, 0.076), which shows promising clinical usability. The average performance (*Avg*) on four lumbar tasks (R-value=0.874, RMSE=0.080, AUC=0.996) shows the overall robustness. We show the sensitivity and specificity in Table II. We achieve high specificity (0.97) and applicable sensitivity (larger than 0.57) for *osteoporosis* classifications on all lumbar tasks. While the *osteopenia* classifications have lower specificity, they have higher sensitivity. As an opportunistic screening tool, our model could provide meaningful alerts for both osteoporosis and osteopenia.

To show the model prediction quality intuitively, we draw the linear fitting curve and the Bland-Altman plot for L1 task in Figure 4. The *intersect* (-0.02, close to 0) and *slop* (1.02, close to 1) of the linear fitting line show the model's good fitness, and the *R-squared* (0.788) measures the closeness between predictions and the ground truth. In the Bland-Altman plot, value errors are drawn against value means for each prediction and ground truth pair. The standard deviation (0.066) further proves the model's balanced performance in the whole data range.

C. The model variants

1) *The Baseline model:* There is no shortage of mature CNNs [26] [48] with the fast development of deep learning in computer vision [24] [49], and we simply employ off-the-shelf CNNs as the *Baseline* model. Since the VGG and Resnet have been shown to work well on hip X-ray BMD estimation [23], they would also solve the chest X-ray BMD estimation. In the *Baseline* model, we adopt VGG16 as feature extractor, we apply the Global Average Pooling (GAP) to reduce spatial dimension, we use two linear layers with *ReLU* non-linearity in the regressor to predict BMD. We use Mean Squared Error (MSE) loss to train the model. In the performance Table I, our proposed model has large improvements over the *baseline* model in all metrics.

2) *The Multi-ROI model (MulROI) :* In order to investigate the effect of the *Transformer Encoder* in the proposed Attentive Multi-ROI model, we replace attentive feature fusion with direct feature concatenation in Figure 2 in the *Multi-ROI* model. The concatenated global feature has the length of 512×15 , and the global regressor now has a larger input dimension. The proposed (*Ours*, Attentive Multi-ROI) model

TABLE I
PERFORMANCE COMPARISON OF DIFFERENT MODELS. VGG16 IS THE FEATURE EXTRACTOR. OUR PROPOSED (THE ATTENTIVE MULTI-ROI MODEL, **Ours**) OUTPERFORMS OTHERS IN ALL FOUR LUMBAR BMD ESTIMATION TASK, IN TERMS OF R-VALUE, RMSE, AUC SCORE.

Model	L1			L2			L3			L4			Avg		
	R-Val	RMSE	AUC	R-val	RMSE	AUC	R-val	RMSE	AUC	R-val	RMSE	AUC	R-val	RMSE	AUC
Baseline	0.866	0.074	0.956	0.870	0.083	0.959	0.863	0.086	0.966	0.822	0.103	0.959	0.855	0.086	0.960
MulPat	0.872	0.071	0.960	0.880	0.079	0.966	0.874	0.083	0.970	0.834	0.096	0.963	0.865	0.082	0.965
AttMulPat	0.879	0.070	0.961	0.882	0.078	0.964	0.873	0.083	0.967	0.838	0.096	0.961	0.868	0.081	0.963
MulRoi	0.883	0.068	0.961	0.887	0.077	0.965	0.877	0.082	0.971	0.838	0.096	0.960	0.871	0.081	0.964
Ours	0.889	0.067	0.963	0.889	0.076	0.964	0.878	0.082	0.971	0.840	0.095	0.966	0.874	0.080	0.966

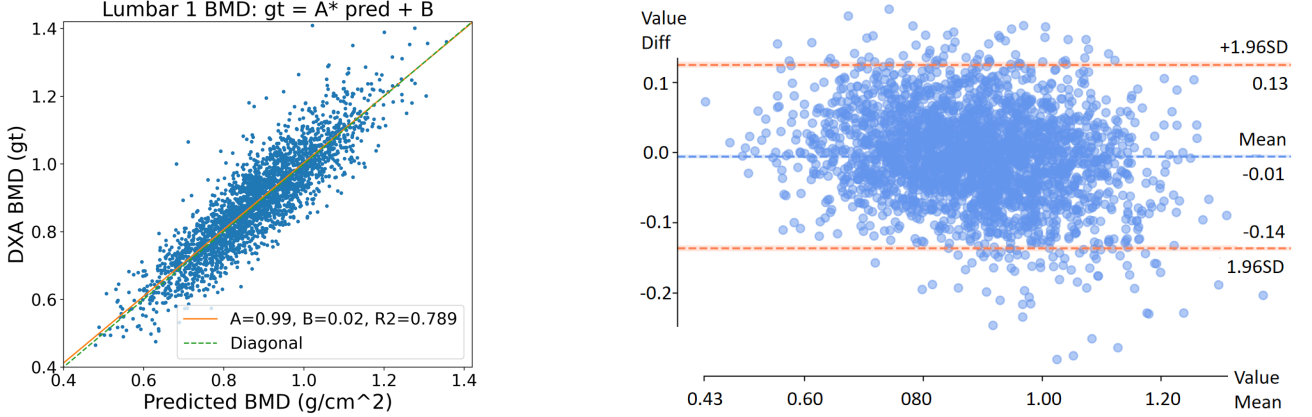


Fig. 4. The linear fitting curve (left) and Bland-Altman plot (right) for the Attentive Multi-ROI model on Lumbar 1 BMD prediction. Model predictions are compared with ground truth. In the linear fitting curve, **A** represents the **slop**, **B** represents the **y-intercept**, **R²** is the coefficient of determination. Each point in the Bland-Altman plot represents a pair of DXA BMD and predicted BMD, the horizontal axis is the mean, and the vertical axis is the difference.

TABLE II
THE ATTENTIVE MULTI-ROI MODEL PREDICTING CHARACTERISTICS USING DIFFERENT THRESHOLD METHODS. SENS, SPEC, ARE SHORT FOR SENSITIVITY, SPECIFICITY RESPECTIVELY. T-SCORE -2.5 IS THE OSTEOPOROSIS THRESHOLD, T-SCORE -1 IS THE OSTEOPENIA THRESHOLD.

Threshold	L1		L2		L3		L4		Avg	
	Sens.	Spec.	Sens.	Spec.	Sens.	Spec.	Sens.	Spec.	Sens.	Spec.
Tscore -2.5	0.66	0.968	0.571	0.978	0.602	0.982	0.521	0.989	0.589	0.979
Tscore -1	0.866	0.838	0.777	0.914	0.796	0.905	0.668	0.927	0.777	0.896

has consistent performance advantages over the *MulRoi* (plain-fusion Multi-ROI) in Table I, demonstrating the positive effect of *Transformer Encoder*.

3) *The Attentive Multi-Patch model (AttMulPat)*: To investigate the benefits of precise ROI extraction in the proposed *Attentive Multi-ROI*, we replace the *landmark-based ROI extraction* with the *image patch splitting* in the *Attentive Multi-Patch* model (*AttMulPat*). We split the high resolution chest X-ray image into evenly distributed patches in Figure 3. Though lacking the precise landmark-based cropping, the *AttMulPat* model is able to learn both individual patch details and inter-patch relations. However, the meaning of content in each patch is less certain. From the comparison of the *AttMulPat* and **Ours** (*AttMulROI*) in Table I, the landmark detection and precise ROIs benefit all four lumbar tasks.

4) *The Multi-Patch model (MulPat)*: To show the effect of *Transformer Encoder* on *Attentive Multi-Patch* model, we train and test the *Multi-Patch* model which instead uses the plain concatenation. Their comparisons in Table I again show that the attention module consistently benefits all four tasks, demonstrating better feature fusion ability.

D. Performance comparisons

To see the advantage of the *Multiple-Modality* working flow in our four models (*MulPat*, *AttMulPat*, *MulRoi*, *AttMulRoi*), we compare them with the *Baseline* in Table I. There exist clear performance superiority of the *Multiple-Modality* models over the *Baseline* since the former could extract not only global patterns but also detailed local textures. The *AttMulPat* model utilizes the simple patch exploration and attentive fusion without complex data pre-processing, and it outperforms the *Baseline* model by a significant margin. The *Baseline* model would need much more training data to reach the similar performance.

The four *Multiple-Modality* models differ from each other by the ROI extraction component and the global fusion component. To see the component-wise boosting effects from the *landmark-based ROI extraction* and the *Transformer Encoder*, four models are compared to each other with the base being the *MulPat* model. Applying the *Transformer Encoder* only (*AttMulPat*) or applying the *landmark-based ROI extraction* only (*MulRoi*) contributes similar amount of benefit to the *MulPat* model in Table I. Applying these two simultaneously in our proposed *AttMulRoi* model leads to the best performance. On the one hand, the precise ROI croppings in the

TABLE III

COMPARISON OF DIFFERENT BACKBONES IN BASELINE MODEL. THE EVALUATION CRITERIA CAN BE FOUND IN THE METRIC SECTION IV-A. VGG16 SHOWS SUPERIOR PERFORMANCES.

Backbone	L1			L2			L3			L4			Avg		
	R-Val	RMSE	AUC	R-val	RMSE	AUC	R-val	RMSE	AUC	R-val	RMSE	AUC	R-val	RMSE	AUC
VGG13	0.864	0.075	0.954	0.865	0.084	0.956	0.862	0.088	0.965	0.828	0.099	0.957	0.855	0.086	0.958
VGG16	0.866	0.074	0.956	0.870	0.083	0.959	0.863	0.086	0.966	0.822	0.103	0.959	0.855	0.086	0.960
VGG19	0.863	0.075	0.955	0.870	0.082	0.958	0.861	0.087	0.961	0.824	0.098	0.960	0.855	0.085	0.958
ResN18	0.831	0.082	0.943	0.846	0.093	0.955	0.835	0.095	0.953	0.794	0.106	0.953	0.826	0.094	0.951
ResN34	0.845	0.078	0.948	0.851	0.088	0.957	0.843	0.092	0.966	0.804	0.105	0.953	0.836	0.091	0.956
ResN50	0.852	0.078	0.949	0.857	0.085	0.961	0.852	0.092	0.964	0.814	0.104	0.957	0.844	0.090	0.958
ResN101	0.846	0.078	0.949	0.860	0.087	0.959	0.855	0.090	0.965	0.805	0.105	0.955	0.841	0.090	0.957

TABLE IV

THE INFLUENCE OF PATCH SPLITTINGS ON MULTI-PATCH MODEL PERFORMANCE. IN FIGURE 3 WE SPLIT THE PATCHES BY DIFFERENT NUMBER OF ROWS AND COLUMNS. A PROPER SPLITTING (3 ROWS BY 3 COLUMNS) LEADS TO BETTER RESULTS.

Patch	L1			L2			L3			L4			Avg		
	R-Val	RMSE	AUC	R-val	RMSE	AUC	R-val	RMSE	AUC	R-val	RMSE	AUC	R-val	RMSE	AUC
2 x 2	0.861	0.075	0.954	0.868	0.082	0.962	0.858	0.088	0.965	0.821	0.100	0.960	0.852	0.086	0.960
3 x 3	0.872	0.071	0.960	0.880	0.079	0.966	0.874	0.083	0.970	0.834	0.096	0.963	0.865	0.082	0.965
4 x 4	0.867	0.073	0.956	0.876	0.080	0.964	0.867	0.085	0.966	0.836	0.096	0.966	0.861	0.083	0.963
Ours	0.889	0.067	0.963	0.889	0.076	0.964	0.878	0.082	0.971	0.840	0.095	0.966	0.874	0.080	0.966

MulRoi and *AttMulRoi* models enable more efficient local texture utilization. On the other hand the plain concatenation in the *MultiPat* and *MulRoi* models treat all the individual ROI features as equal which renders the model less robust to occlusion or noises, especially in case of implants or tissue consolidations. The *Transformer Encoder* adjusts the individual features in a learnable and flexible way, addressing the correlations among chest bones, which leads to better ROI feature robustness.

E. Ablation study

1) *Convolutional backbone selection*: To find the best convolutional backbones for extracting BMD features, we compare VGG13, VGG16, VGG19, Resnet18, Resnet34, Resnet50 [50] [26] with the *Baseline* pipeline. The input modalities have a fixed resolution of (256, 256). In Table III, VGG16 and VGG19 outperform other backbones in most metrics demonstrating better ability at extracting BMD information in the chest X-ray images. The VGG family in general surpass Resnet variants in all tasks, suggesting that relatively simple backbones work better on bone texture recognition. The proper combination of convolutional kernels and backbone depth in VGG16 exploits the X-ray density patterns more effectively, and we use VGG16 as the default feature extractor in all experiments.

2) *Image splitting dimension for the Multi-Patch model*: In the *Multi-Patch* model, we split the original chest X-ray image into evenly split patches in Figure 3. To find out the best patch splitting dimensions, we train and test the *Multi-Patch* model under different dimensions. We try different split dimension N (N rows by N columns), and summarize the performance comparison in Table IV. Smaller split dimensions (e.g., $N = 2$) produce patches covering a larger field of view with more content, impeding detailed texture exploration. Larger split dimensions (e.g., $N = 4$) produce patches covering a smaller area, resulting in theme shifting of each patches because of the varied shape, size, and positions in chest X-ray. As a result,

$N=3$ produce the best performance and we use $N=3$ as default for the *Multi-Patch* models.

V. DISCUSSION

1) *Osteoporosis threshold applicability*: While the R-value and RMSE are direct error measures of the predictions, AUC scores evaluate osteoporosis classification quality. But there are contradictions between the value-comparing metric (R-value, RMSE) and the binary-classifying metric (AUC) when evaluating our proposed *Attentive Multi-ROI* model on (L1, L2) versus on (L3, L4) in Table I. It performs better on the L3 and L4 than on the L1 and L2 using the AUC score metric, while it performs better on L1 and L2 in terms of R-value or RMSE. To investigate this discrepancy, we draw the *ROC AUC* in Figure 6. At each False Positive Rate (FPR), L3 and L4 have higher True Positive Rate (TPR) than L1 and L2. This comes from the fact that L3 and L4 have consistently larger BMD averages in Figure 5 thus having less osteoporosis cases under the same judging threshold. Therefore, the AUC scores for L3 and L4 should not be compared directly to L1 or L2.

To investigate the appropriate thresholds for different lumbar tasks, we analyze their differences in the Figure 6. When applying the fixed threshold of -2.5 on predictions, four tasks have distinct performances (the marked points in the yellow box). L4 has much smaller TPR and FPR than L1, due to the drawback of applying uniform threshold across all vertebrae. Similar observation can be seen for applying uniform threshold of -1 (marked points in the lime box). In short, each bone should have a separate threshold due to its location and burden distinction in the human body. One way to compensate this discrepancy is to produce probabilistic warnings using both -2.5 and -1 on all four lumbar vertebrae. Another way is to use relative thresholds such as *Last 10%* and *Last 20%*. Absolute thresholds stick to rigid standards, while relative thresholds produce flexible references according to ranks in the whole population.

2) *The ground truth distribution*: The dataset has large variations in sample counts and BMD averages for different

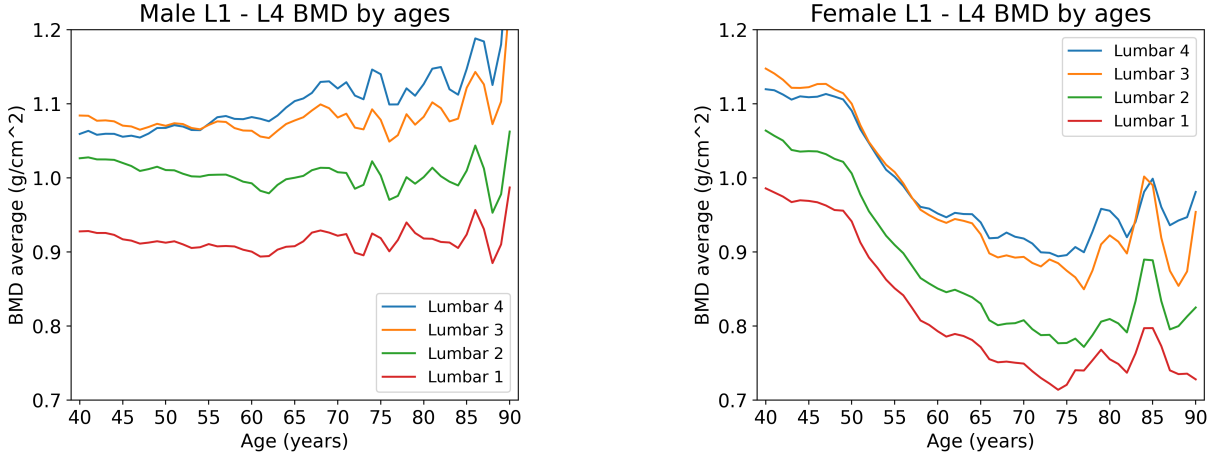


Fig. 5. DXA BMD averages across ages for both genders. Different vertebrae (L1, L2, L3, L4) are drawn separately.

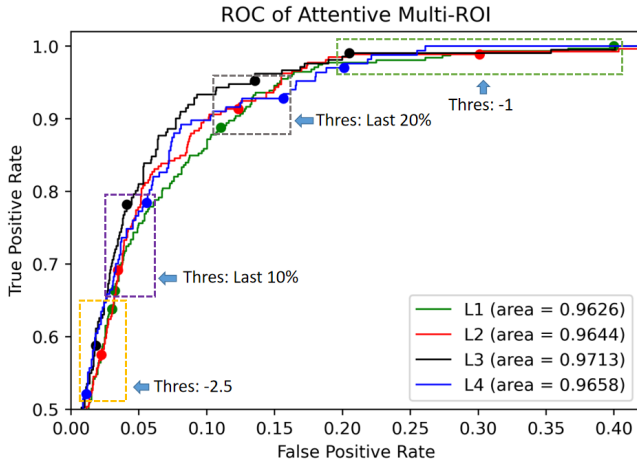


Fig. 6. The Receiver Operating Characteristic (ROC) Area Under Curve (AUC) of the proposed *Attentive Multi-ROI* model on four lumbar BMD tasks (L1, L2, L3, L4). We only draw the upper left part of the whole AUC curve. The T-score -2.5 is used as osteoporosis threshold to binarize the ground truth. Applying sample-wise thresholds on the prediction produces the points in the curves. The orange box contains marked points of applying T-score threshold -2.5 on predictions, the lime box is for threshold -1. The violet box markers represent the *last 10%* thresholds (separate thresholds for different lumbar vertebra), and the grey box is for *last 20%*. The X-axis (FPR) and Y-axis (TPR) are for osteoporosis classification.

ages. From 45 to 60, each age has more than 200 samples for both genders. However above 75 years, each age has less than 30 samples for either genders. This unbalanced sample distribution may lead to biased predictions for particular age groups.

To show the ground truth distribution, we draw the BMD averages against ages in Figure 5. Under age 50, both males and females have stable BMD distributions, but females have higher BMD averages. Under age 70, male BMD averages change little, while female BMD averages drop greatly. Above the age of 70, the BMD averages fluctuates for both sex partly due to sample insufficiency. Considering there are fewer cases above 70, more care are needed for the interpretation.

3) *Result analysis by sex/age groups*: To analyze the performance in each age/sex groups, the data results are split into 8 separate zones by sex and age in Table V. Due to the large BMD variations in ages, R-value may not be fairly comparable between groups while RMSE may be more objective. From the RMSE point of view, *F40-70* gets the best performance compared to other groups in all lumbar tasks, while *F70-90* gets the worst performance. From the osteoporosis alarming perspective, all the male groups get relatively higher AUC scores, while the female groups get lower AUC scores especially for older ages. The interpretations are subject to clinical scrutiny because of the osteoporosis threshold applicability mentioned in Section V-1 and the distribution variations in Section V-2.

4) *The possible upper bound for model performance* : We derive the possible performance upper bound from the ground truth (DXA BMD). The ground truth Pearson correlations between each lumbar vertebra pair are listed in Table VI. The R-value between L1 and L3 is 0.8775, while the R-value between L2 and L3 is 0.9311. The longer distance of the vertebra pair, the smaller R-value. Our proposed model has a R-value of 0.8885 on L1 predictions and 0.8776 on L3 predictions, larger than the DXA BMD R-value between L1 and L3. Considering the approximation between L1 and L3, the chest X-Ray may not be significantly better than either of them at providing references. This means our model adequately utilizes physiological information of the chest X-ray bones. The same observation can be drawn between L2 and L4, where our model provides better reference than themselves. As for the RMSE between each vertebra pair in Table VII, the model provides much better references than a neighboring vertebra does. This further proves the promising applicability of the proposed model.

5) *Prediction interpretation limitations*: Although CNN and transformer modules have been successfully applied in many vision and language tasks, more caution should be taken for medical tasks. From a single chest X-ray scan, even medical experts are not able to get clear BMD evidence. The BMD patterns and bone texture information are not immediately

TABLE V

THE *Attentive Multi-ROI* PERFORMANCE IN DIFFERENT SEX/AGE GROUPS. M/F IS SHORT FOR MALE/FEMALE, 40-50 MEANS THE AGE OF 40 TO 50.

Patch	L1			L2			L3			L4			Avg		
	R-Val	RMSE	AUC	R-val	RMSE	AUC	R-val	RMSE	AUC	R-val	RMSE	AUC	R-val	RMSE	AUC
All	0.888	0.067	0.963	0.889	0.076	0.964	0.878	0.082	0.971	0.840	0.095	0.966	0.874	0.080	0.966
M40-50	0.845	0.067	0.980	0.848	0.076	0.992	0.842	0.080	0.990	0.822	0.085	0.947	0.839	0.077	0.977
M50-60	0.866	0.065	0.940	0.857	0.076	0.926	0.844	0.080	0.955	0.801	0.094	0.955	0.842	0.079	0.944
M60-70	0.820	0.077	0.978	0.795	0.089	0.972	0.779	0.101	0.922	0.726	0.116	0.994	0.780	0.095	0.966
M70-90	0.884	0.077	0.980	0.876	0.091	0.977	0.851	0.103	0.966	0.833	0.115	0.953	0.861	0.096	0.969
F40-50	0.871	0.060	0.970	0.866	0.068	0.983	0.870	0.070	0.997	0.838	0.083	0.978	0.861	0.070	0.982
F50-60	0.897	0.060	0.946	0.904	0.064	0.948	0.896	0.071	0.958	0.864	0.085	0.943	0.890	0.070	0.949
F60-70	0.882	0.065	0.931	0.889	0.074	0.932	0.886	0.080	0.936	0.820	0.104	0.926	0.869	0.081	0.931
F70-90	0.798	0.093	0.873	0.777	0.098	0.878	0.805	0.106	0.883	0.777	0.120	0.912	0.789	0.104	0.886

TABLE VI

R-VALUE BETWEEN VERTEBRA PAIRS IN THE GROUND TRUTH

R-values	L1	L2	L3	L4
L1	1.000	0.918	0.878	0.807
L2	0.918	1.000	0.931	0.836
L3	0.878	0.931	1.000	0.898
L4	0.807	0.836	0.898	1.000

TABLE VII

RMSE BETWEEN VERTEBRA PAIRS IN THE GROUND TRUTH

RMSE	L1	L2	L3	L4
L1	0.000	0.101	0.177	0.192
L2	0.101	0.000	0.101	0.129
L3	0.177	0.101	0.000	0.079
L4	0.192	0.129	0.079	0.000

visible by human eyes. In our experiments the correlation between chest X-ray image and lumbar DXA BMD is established through training machine learning models, the principles of which have not been verified strictly as for now. The black-box process brings about uncertainty for special cases not sufficiently trained on [31].

For formal judgement of osteoporosis or osteopenia, only DXA BMD on the lumbar or hip should be considered [9] [10]. Model BMD prediction from chest X-ray works as low-cost and opportunistic way. It could not confidently determine osteoporosis status, and the patient should take hip/lumbar DXA scans in cases of positive alerts. For older people, hip BMD is recommended since it is more reliable for old population (older than 70) or with spine diseases. Certain population such as post-menopause female or male older than 70 have more risks, and should take comprehensive examination by medical experts [10].

VI. CONCLUSION

In this paper, we design deep learning models to estimate lumbar bone mineral density using chest X-ray images. We propose the anatomy-aware *Attentive Multi-ROI* model that can extract local bone textures and generate robust global representation through the *Transformer Encoder*. The landmark-based ROI extraction promotes the local feature robustness against scanning variations. The self-attention based transformer encoder improves the system reliability in case of noises, occlusions. Our proposed *Attentive Multi-ROI* model shows good performance on four lumbar BMD tasks, and it makes useful osteoporosis judgements. Through extensive

experiments and analysis, we show our model has great clinical potential for opportunistic osteoporosis screening and alarming.

REFERENCES

- [1] T. Sözen, L. Özışık, and N. Ç. Başaran, "An overview and management of osteoporosis," *European journal of rheumatology*, vol. 4, no. 1, p. 46, 2017.
- [2] E. M. Lewiecki, D. Leader, R. Weiss, and S. A. Williams, "Challenges in osteoporosis awareness and management: results from a survey of US postmenopausal women," *Journal of Drug Assessment*, vol. 8, no. 1, pp. 25–31, 2019.
- [3] A. D. Smith, "Screening of bone density at CT: an overlooked opportunity," 2019.
- [4] X. Cheng, K. Zhao, X. Zha, X. Du, Y. Li, S. Chen, Y. Wu, S. Li, Y. Lu, Y. Zhang *et al.*, "Opportunistic Screening Using Low-Dose CT and the Prevalence of Osteoporosis in China: A Nationwide, Multicenter Study," *Journal of Bone and Mineral Research*, 2020.
- [5] N. Dagan, E. Elnekave, N. Barda, O. Bregman-Amitai, A. Bar, M. Orlovsky, E. Bachmat, and R. D. Balicer, "Automated opportunistic osteoporotic fracture risk assessment using computed tomography scans to aid in FRAX underutilization," *Nature Medicine*, vol. 26, no. 1, pp. 77–82, 2020.
- [6] S. Jang, P. M. Graffy, T. J. Ziemlewicz, S. J. Lee, R. M. Summers, and P. J. Pickhardt, "Opportunistic osteoporosis screening at routine abdominal and thoracic CT: normative L1 trabecular attenuation values in more than 20 000 adults," *Radiology*, vol. 291, no. 2, pp. 360–367, 2019.
- [7] P. J. Pickhardt, P. M. Graffy, R. Zea, S. J. Lee, J. Liu, V. Sandfort, and R. M. Summers, "Automated abdominal CT imaging biomarkers for opportunistic prediction of future major osteoporotic fractures in asymptomatic adults," *Radiology*, vol. 297, no. 1, pp. 64–72, 2020.
- [8] F. Wang, K. Zheng, Y. Wang, X. Zhou, L. Lu, J. Xiao, M. Wu, C.-F. Kuo, and S. Miao, "Opportunistic screening of osteoporosis using plain film chest x-ray," in *Predictive Intelligence in Medicine*, I. Rekik, E. Adeli, S. H. Park, and J. Schnabel, Eds. Cham: Springer International Publishing, 2021, pp. 138–146.
- [9] W. H. Organization *et al.*, *Assessment of fracture risk and its application to screening for postmenopausal osteoporosis: report of a WHO study group [meeting held in Rome from 22 to 25 June 1992]*. World Health Organization, 1994.
- [10] J. E. Compston, A. L. Cooper, C. Cooper, N. Gittoes, C. L. Gregson, N. C. Harvey, S. Hope, J. A. Kanis, E. V. McCloskey, K. E. S. Poole, D. M. Reid, P. Selby, F. Thompson, A. Thurston, and N. Vine, "UK clinical guideline for the prevention and treatment of osteoporosis," *Archives of Osteoporosis*, vol. 12, 2017.
- [11] B. C. Silva, W. D. Leslie, H. Resch, O. Lamy, O. M. Lesnyak, N. Binkley, E. V. McCloskey, J. A. Kanis, and J. P. Bilezikian, "Trabecular bone score: A noninvasive analytical method based upon the dxa image," *Journal of Bone and Mineral Research*, vol. 29, 2014.
- [12] V. Bousson, C. Bergot, B. Sutter, P. Levitz, B. Cortet, and the Scientific Committee of the Grio, "Trabecular bone score (tbs): available knowledge, clinical relevance, and future prospects," *Osteoporosis International*, vol. 23, pp. 1489–1501, 2011.
- [13] N. C. Harvey, C. C. Glüer, N. Binkley, E. V. McCloskey, M. Brandi, C. Cooper, D. Kendler, O. Lamy, A. Laslop, B. M. Camargos, J. Reingster, R. Rizzoli, and J. A. Kanis, "Trabecular bone score (tbs) as a new complementary approach for osteoporosis evaluation in clinical practice." *Bone*, vol. 78, pp. 216–24, 2015.

- [14] S. Boutroy, M. L. Bouxsein, F. Munoz, and P. D. Delmas, "In vivo assessment of trabecular bone microarchitecture by high-resolution peripheral quantitative computed tomography." *The Journal of clinical endocrinology and metabolism*, vol. 90 12, pp. 6508–15, 2005.
- [15] J. J. Schreiber, P. A. Anderson, H. G. Rosas, A. L. Buchholz, and A. G. Au, "Hounsfield units for assessing bone mineral density and strength: a tool for osteoporosis management." *The Journal of bone and joint surgery. American volume*, vol. 93 11, pp. 1057–63, 2011.
- [16] J. E. Adams, "Quantitative computed tomography." *European journal of radiology*, vol. 71 3, pp. 415–24, 2009.
- [17] S. Lee, C. K. Chung, S. Oh, and S. B. Park, "Correlation between bone mineral density measured by dual-energy x-ray absorptiometry and hounsfield units measured by diagnostic ct in lumbar spine," *Journal of Korean Neurosurgical Society*, vol. 54, pp. 384 – 389, 2013.
- [18] Y.-L. Li, K. H. Wong, M. W.-M. Law, B. X.-H. Fang, V. W. H. Lau, V. V. Vardhanabuti, V. K.-H. Lee, A. K.-C. Cheng, W. yin Ho, and W. W. M. Lam, "Opportunistic screening for osteoporosis in abdominal computed tomography for chinese population," *Archives of Osteoporosis*, vol. 13, pp. 1–7, 2018.
- [19] E. Alacreu, D. Moratal, and E. Arana, "Opportunistic screening for osteoporosis by routine ct in southern europe," *Osteoporosis International*, vol. 28, pp. 983–990, 2016.
- [20] B. Specker and E. Schoenau, "Quantitative bone analysis in children: current methods and recommendations." *The Journal of pediatrics*, vol. 146 6, pp. 726–31, 2005.
- [21] Baroncelli and I. Giampiero, "Quantitative ultrasound methods to assess bone mineral status in children: Technical characteristics, performance, and clinical application," *Pediatric Research*, vol. 63, no. 3, p. 220, 2008.
- [22] P. Pisani, M. D. Renna, F. Conversano, E. Casciaro, M. Muratore, E. Quarta, M. D. Paola, and S. Casciaro, "Screening and early diagnosis of osteoporosis through x-ray and ultrasound based techniques." *World journal of radiology*, vol. 5 11, pp. 398–410, 2013.
- [23] K. Zheng, Y. Wang, X.-Y. Zhou, F. Wang, L. Lu, C. Lin, L. Huang, G. Xie, J. Xiao, C.-F. Kuo, and S. Miao, "Semi-supervised learning for bone mineral density estimation in hip x-ray images," in *Medical Image Computing and Computer Assisted Intervention – MICCAI 2021*, M. de Bruijne, P. C. Cattin, S. Cotin, N. Padoy, S. Speidel, Y. Zheng, and C. ESSERT, Eds. Cham: Springer International Publishing, 2021, pp. 33–42.
- [24] J. Deng, W. Dong, R. Socher, L.-J. Li, K. Li, and L. Fei-Fei, "Imagenet: A large-scale hierarchical image database," in *2009 IEEE Conference on Computer Vision and Pattern Recognition*, 2009, pp. 248–255.
- [25] C. Szegedy, W. Liu, Y. Jia, P. Sermanet, S. Reed, D. Anguelov, D. Erhan, V. Vanhoucke, and A. Rabinovich, "Going deeper with convolutions," in *2015 IEEE Conference on Computer Vision and Pattern Recognition (CVPR)*, 2015, pp. 1–9.
- [26] K. He, X. Zhang, S. Ren, and J. Sun, "Deep residual learning for image recognition," *CoRR*, vol. abs/1512.03385, 2015. [Online]. Available: <http://arxiv.org/abs/1512.03385>
- [27] M. Tan and Q. V. Le, "Efficientnet: Rethinking model scaling for convolutional neural networks," *ArXiv*, vol. abs/1905.11946, 2019.
- [28] O. Ronneberger, P. Fischer, and T. Brox, "U-net: Convolutional networks for biomedical image segmentation," in *Medical Image Computing and Computer-Assisted Intervention – MICCAI 2015*, N. Navab, J. Hornegger, W. M. Wells, and A. F. Frangi, Eds. Cham: Springer International Publishing, 2015, pp. 234–241.
- [29] H.-C. Shin, L. Lu, L. Kim, A. Seff, J. Yao, and R. M. Summers, "Interleaved text/image deep mining on a large-scale radiology database," in *2015 IEEE Conference on Computer Vision and Pattern Recognition (CVPR)*, 2015, pp. 1090–1099.
- [30] K. Yan, X. Wang, L. Lu, and R. M. Summers, "Deeplesion: automated mining of large-scale lesion annotations and universal lesion detection with deep learning," *Journal of Medical Imaging*, vol. 5, 2018.
- [31] R. Yamashita, M. Nishio, R. K. G. Do, and K. Togashi, "Convolutional neural networks: an overview and application in radiology," *Insights into Imaging*, vol. 9, pp. 611 – 629, 2018.
- [32] X. Wang, R. Girshick, A. Gupta, and K. He, "Non-local neural networks," in *2018 IEEE/CVF Conference on Computer Vision and Pattern Recognition (CVPR)*. Los Alamitos, CA, USA: IEEE Computer Society, jun 2018, pp. 7794–7803. [Online]. Available: <https://doi.ieeecomputersociety.org/10.1109/CVPR.2018.00813>
- [33] I. Bello, B. Zoph, Q. Le, A. Vaswani, and J. Shlens, "Attention augmented convolutional networks," in *2019 IEEE/CVF International Conference on Computer Vision (ICCV)*, 2019, pp. 3285–3294.
- [34] A. Dosovitskiy, L. Beyer, A. Kolesnikov, D. Weissenborn, X. Zhai, T. Unterthiner, M. Dehghani, M. Minderer, G. Heigold, S. Gelly, J. Uszkoreit, and N. Houlsby, "An image is worth 16x16 words: Transformers for image recognition at scale," in *International Conference on Learning Representations*, 2021. [Online]. Available: <https://openreview.net/forum?id=YicbFdNTTy>
- [35] J. Hu, L. Shen, and G. Sun, "Squeeze-and-excitation networks," in *2018 IEEE/CVF Conference on Computer Vision and Pattern Recognition*, 2018, pp. 7132–7141.
- [36] Z. Huang, X. Wang, L. Huang, C. Huang, Y. Wei, and W. Liu, "Ccnet: Criss-cross attention for semantic segmentation," in *Proceedings of the IEEE/CVF International Conference on Computer Vision (ICCV)*, October 2019.
- [37] H. Hu, Z. Zhang, Z. Xie, and S. C.-F. Lin, "Local relation networks for image recognition," *2019 IEEE/CVF International Conference on Computer Vision (ICCV)*, pp. 3463–3472, 2019.
- [38] Y. Cao, J. Xu, S. Lin, F. Wei, and H. Hu, "Gcnet: Non-local networks meet squeeze-excitation networks and beyond," in *2019 IEEE/CVF International Conference on Computer Vision Workshop (ICCVW)*, 2019, pp. 1971–1980.
- [39] H. Hu, J. Gu, Z. Zhang, J. Dai, and Y. Wei, "Relation networks for object detection," *2018 IEEE/CVF Conference on Computer Vision and Pattern Recognition*, pp. 3588–3597, 2018.
- [40] A. Vaswani, N. Shazeer, N. Parmar, J. Uszkoreit, L. Jones, A. N. Gomez, L. u. Kaiser, and I. Polosukhin, "Attention is all you need," in *Advances in Neural Information Processing Systems*, I. Guyon, U. V. Luxburg, S. Bengio, H. Wallach, R. Fergus, S. Vishwanathan, and R. Garnett, Eds., vol. 30. Curran Associates, Inc., 2017. [Online]. Available: <https://proceedings.neurips.cc/paper/2017/file/3f5ee243547dee91fbd053c1c4a845aa-Paper.pdf>
- [41] J. Devlin, M.-W. Chang, K. Lee, and K. Toutanova, "BERT: Pre-training of deep bidirectional transformers for language understanding," in *Proceedings of the 2019 Conference of the Association for Computational Linguistics: Human Language Technologies, Volume 1 (Long and Short Papers)*. Minneapolis, Minnesota: Association for Computational Linguistics, Jun. 2019, pp. 4171–4186. [Online]. Available: <https://aclanthology.org/N19-1423>
- [42] A. Radford, J. Wu, R. Child, D. Luan, D. Amodei, and I. Sutskever, "Language models are unsupervised multitask learners," 2019.
- [43] T. B. Brown, B. Mann, N. Ryder, M. Subbiah, J. Kaplan, P. Dhariwal, A. Neelakantan, P. Shyam, G. Sastry, A. Askell, S. Agarwal, A. Herbert-Voss, G. Krueger, T. J. Henighan, R. Child, A. Ramesh, D. M. Ziegler, J. Wu, C. Winter, C. Hesse, M. Chen, E. Sigler, M. Litwin, S. Gray, B. Chess, J. Clark, C. Berner, S. McCandlish, A. Radford, I. Sutskever, and D. Amodei, "Language models are few-shot learners," *ArXiv*, vol. abs/2005.14165, 2020.
- [44] K. Han, Y. Wang, H. Chen, X. Chen, J. Guo, Z. Liu, Y. Tang, A. Xiao, C. Xu, Y. Xu, Z. Yang, Y. Zhang, and D. Tao, "A survey on visual transformer," *ArXiv*, vol. abs/2012.12556, 2020.
- [45] S. H. Khan, M. Naseer, M. Hayat, S. W. Zamir, F. S. Khan, and M. Shah, "Transformers in vision: A survey," *arXiv preprint arXiv:2101.01169*, 2021.
- [46] M. Chen, A. Radford, J. Wu, H. Jun, P. Dhariwal, D. Luan, and I. Sutskever, "Generative pretraining from pixels," in *ICML*, 2020.
- [47] W. Li, Y. Lu, K. Zheng, H. Liao, C. Lin, J. Luo, C.-T. Cheng, J. Xiao, L. Lu, C.-F. Kuo *et al.*, "Structured landmark detection via topology-adapting deep graph learning," *arXiv preprint arXiv:2004.08190*, 2020.
- [48] K. Simonyan and A. Zisserman, "Very deep convolutional networks for large-scale image recognition," *CoRR*, vol. abs/1409.1556, 2014. [Online]. Available: <http://arxiv.org/abs/1409.1556>
- [49] Y. LeCun, Y. Bengio, and G. Hinton, "Deep learning," *Nature*, vol. 521, pp. 436–44, 05 2015.
- [50] K. Simonyan and A. Zisserman, "Very deep convolutional networks for large-scale image recognition," in *International Conference on Learning Representations*, 2015.